Time-resolved study of nonlinear three-magnon processes in yttrium iron garnet films

H. J. Jason Liu,[1,2] Grant A. Riley,[1] César L. Ordóñez-Romero,[3] Boris A. Kalinikos,[4] and Kristen S. Buchanan[1,*]

[1]*Department of Physics, Colorado State University, Fort Collins, Colorado 80523, USA*

[2]*Department of Physics and Astronomy, Georgia Southern University, Statesboro, Georgia 30460, USA*

[3]*Instituto de Física, Universidad Nacional Autónoma de México, Ciudad Universitaria 04510, México*

[4]*St. Petersburg Electrotechnical University, St. Petersburg 197376, Russia*

(Received 31 October 2018; published 25 January 2019)

In this work, the temporal aspects of two nonlinear spin-wave processes, i.e., three-magnon splitting and confluence, were investigated in a yttrium iron garnet film. Three-magnon splitting involves the conversion of a magnon at the microwave pumping frequency f_p into two magnons, each with a frequency near $f_p/2$, while confluence refers to the subsequent combination of two of the split magnons into one with frequency $f_c < f_p$. Time-resolved Brillouin scattering measurements confirm that these processes occur close to the driving antenna ($<$1.7 mm away), which is expected. The data indicate, however, that magnons with larger group velocities are more likely to undergo confluence, which is not predicted by existing theory. Understanding the details of the splitting and confluence processes may have important implications for the use of short-wavelength spin waves for spintronic devices.

DOI: 10.1103/PhysRevB.99.024429

The dynamics of a wide range of physical systems including fluids, climate, and weather are intrinsically nonlinear. Magnetic materials, especially low-loss yttrium iron garnet (YIG) films, provide an accessible model system for the study of these processes. The study of nonlinear magnetization dynamics dates back to the early 1950s when experiments showed that resonances of the electrons in ferromagnetic materials are considerably more complex than those of nuclear spins [1]. Subsequent work has uncovered a rich array of phenomena that includes foldover, instabilities and chaotic behaviors [2], solitary waves, and nonlinear processes have also been exploited to create and study Bose-Einstein condensates of magnons [3]. Three-magnon processes, a type of first-order Suhl instability [4–6], are presently of considerable interest because recent work shows that short-wavelength spin waves generated by parametric pumping can be used to effectively generate spin currents for nanoscale spintronic devices [7–14].

Splitting and confluences are both three-magnon processes, where the former involves the splitting of a magnon at the pumping frequency f_p into two, both with frequencies near $f_p/2$, while the latter is the inverse process where two split or $f_p/2$ magnons combine into a magnon with frequency f_c. For both processes, energy and momentum must be conserved. Experiments conducted in the 1970s on single-crystal YIG spheres showed that both three- and four-magnon processes, where three-magnon splitting and confluence were both considered, must be accounted for to explain experimental measurements of spin-wave linewidths made for a range of wave vectors [15,16]. More recent studies done using Brillouin light scattering (BLS) have shown that the wave-vector range of the split magnons as a function of power [17] and angle [18] agrees well with predictions based on the linear dispersion relations. Direct observation of the confluence signal was first reported in Ref. [18], where BLS measurements showed that the confluence magnons have small wave vectors, which also agrees with dispersion theory. Time- and space-resolved BLS measurements made in a surface wave configuration [17] provided some insight into the spatial characteristics of the $f_p/2$ signal, but open questions remain, especially regarding the details of the timing of the splitting and confluence processes.

In this work, time- and space-resolved BLS was used to investigate the three-magnon splitting and confluence processes in a YIG film. Analysis of the time-resolved signals provides insight into when and where these processes occur, and which magnons participate in the confluence process.

Spin waves were excited in a YIG film with a width, length, and thickness of 2.2 mm, 37 mm, and 11.6 μm, respectively, using a 50-μm-wide microwave stripline antenna. The YIG film is single crystal, prepared by liquid phase epitaxy. A static magnetic field of $H = 337$ Oe was applied parallel to the long axis of the YIG film (Fig. 1). Magnons were driven at a pumping frequency of $f_p = 2.5$ GHz (referred to as f_p magnons). This is expected to generate split ($f_p/2$) magnons near 1.25 GHz, which is just above the low-frequency cutoff of the dispersion relations [Fig. 2(a)]. A microwave pulse with a 5 μs duration, 40 kHz repetition rate, and power of 575 mW was used. This is above the nonlinear power threshold of 200 μW for this field-frequency combination, which was determined by network analyzer measurements (not shown). This pumping power, which is considerably larger than the threshold power, was chosen to increase the confluence signal so that it could be more easily observed in the time-resolved measurements; a low repetition rate was used to minimize heating effects. The generated magnons were detected using time- and space-resolved BLS in a forward-scattering configuration [19]. The incident light (532 nm, $\sim$80 mW) was

*Kristen.Buchanan@colostate.edu

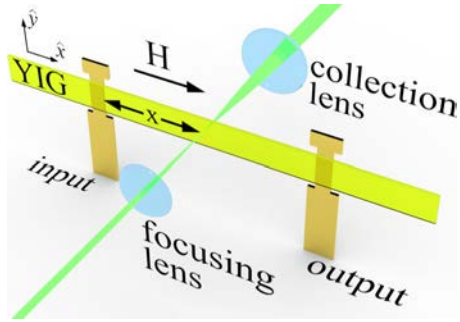

FIG. 1. Illustration of the BLS setup. The external magnetic field H was applied along the long axis of the YIG film and the BLS probe spot was centered on the film width and scanned along x.

focused down to ∼60 μm onto the surface of the YIG film a distance x from the antenna (Fig. 1). This distance was varied from 2.75 to 4.00 mm, where 2.75 mm was the closest x that could be measured without partially blocking the beam with the sample holder. The scattered light was analyzed using a six-pass tandem Fabry-Perot interferometer with time-of-flight tagging to obtain a measure of the magnon populations vs frequency with a temporal resolution of 2 ns.

The splitting and confluence processes can be understood by examining the spin-wave dispersion relations. Dispersion relations, calculated following the method outlined in Ref. [20], which uses a dipole-exchange formulation of the theory that allows for solutions for all spin-wave propagation angles, are shown in Fig. 2(a). Material parameters typical for YIG [21] were used: gyromagnetic ratio of 2.8 MHz/Oe, saturation magnetization of 1830 G, and exchange constant of 3×10^{-12} cm^2. The dispersion relations shown here are for a thin film of infinite extent, which is a good approximation for the millimeter-sized YIG strip used here. To conserve energy, the frequencies of the split magnons must sum to f_p and hence can range from the lowest possible available state in the dispersion relation, 0.98 GHz, up to 1.52 GHz [cross-hatched region in Fig. 2(a)]. To conserved momentum, the split magnons will have antiparallel wave vectors. Experimentally, confluence magnons have been observed with $f_c < f_p$ and with small but nonzero wave vectors [18]. Figure 2(a) shows projections of the dispersion relations along x, but other magnons allowed by the full spin-wave manifold may also participate in these processes.

Figure 2(b) shows a time-integrated BLS spectrum for $x =$ 2.75 mm, where the peaks observed at 2.5, 1.25, and 2.2 GHz correspond to the f_p, $f_p/2$, and f_c magnons, respectively, and agree well with the frequencies reported in Ref. [18]. The data shown here were extracted from the anti-Stokes side of the spectrum since the anti-Stokes scattering signals were stronger than the Stokes, which is typical for magnon BLS spectra in YIG [22]. The $f_p/2$ signal is large compared to that observed at f_p because the majority of the f_p magnons undergo splitting. The corresponding time-resolved BLS data [Fig. 2(c)] show that the f_p signal arrives first and has a sizable amplitude for the first 30 ns and a much weaker amplitude for the remainder of the microwave pulse, which is typical for a nonlinear spin-wave process [23]. The strong initial peak corresponds to a period where the magnon population grows

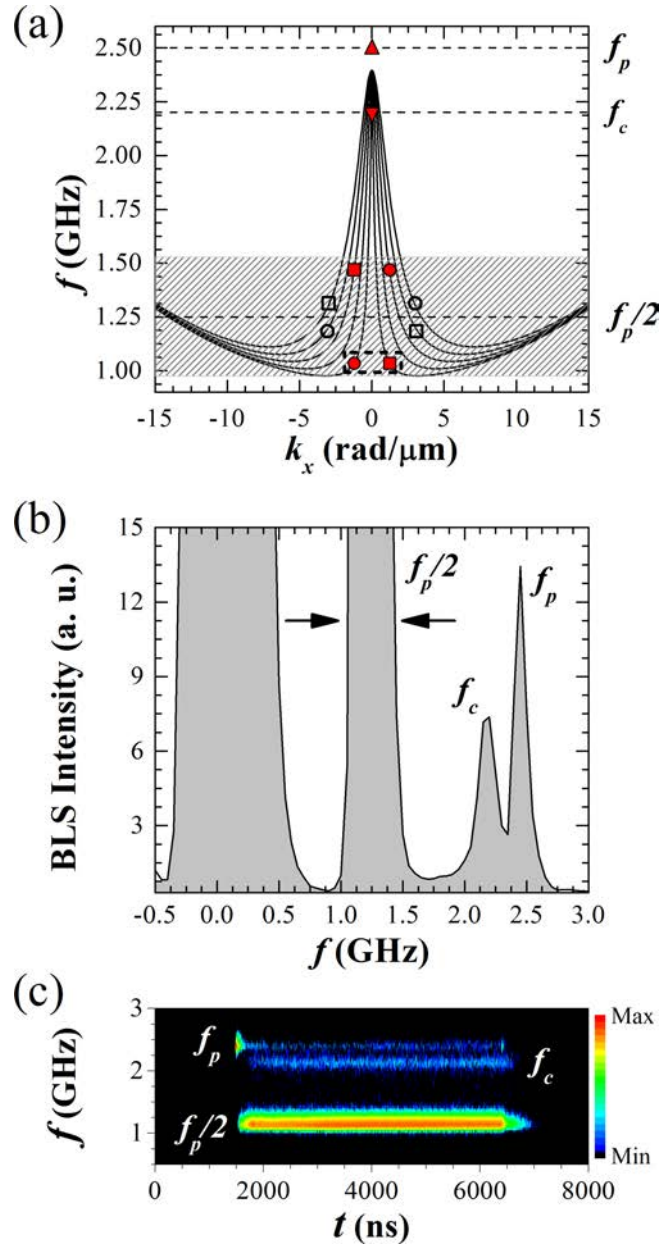

FIG. 2. (a) Dispersion relations for the first five spin-wave modes calculated along the x direction. Dashed lines show f_p, $f_p/2$, and f_c and the cross-hatched region represents the frequency range for magnons that can form by splitting. An f_p magnon (red up-triangle) will split into two magnons with antiparallel wave vectors and frequencies that sum to f_p (each pair of symbols represents a possible split pair). The dashed rectangular box shows a magnon pair that can undergo confluence to $f_c < f_p$ (red square and circle). The (b) time-integrated and (c) time-resolved BLS spectra at $x = 2.75$ mm show signals at each f_p, $f_p/2$, and f_c.

and eventually reaches the nonlinear threshold. The $f_p/2$ and the f_c signals arrive later and show a more gradual increase in intensity and a slower decay after the pulse ends.

Figure 3 shows the integrated BLS intensities as a function of time t for selected x, where the intensities were integrated from 2.3–2.7, 1.0–1.5, and 2.1–2.3 GHz for the f_p, $f_p/2$, and f_c magnon populations, respectively. The f_p signal [Fig. 3(a)]

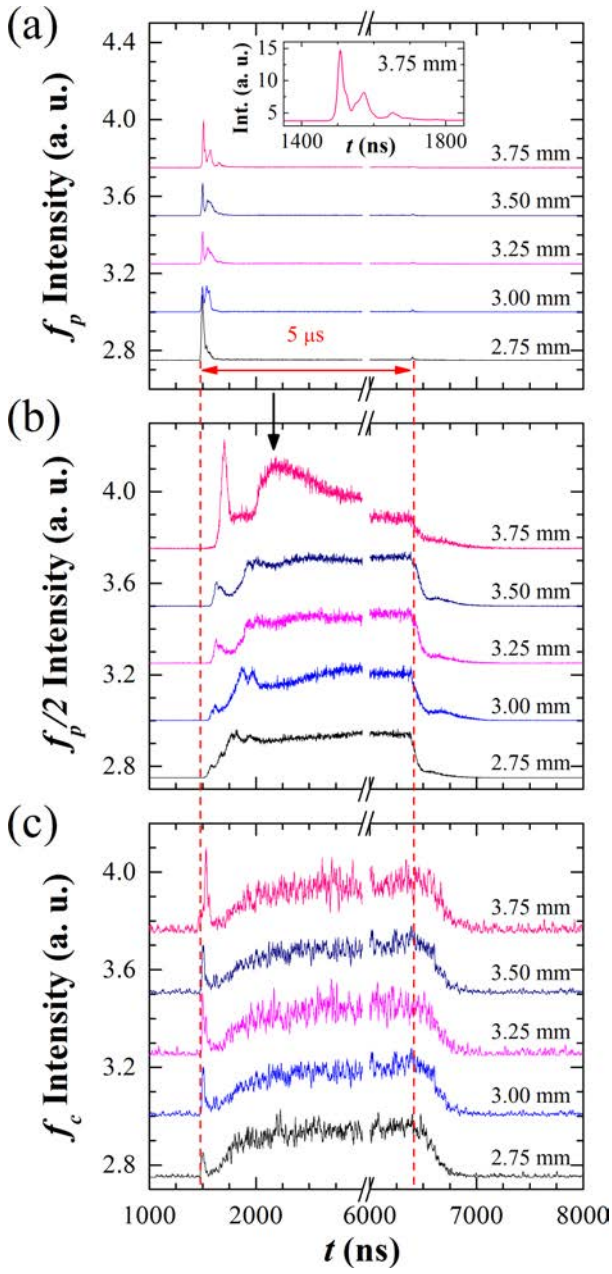

FIG. 3. Integrated (a) f_p, (b) $f_p/2$, and (c) f_c magnon signals vs time t at selected x. The intensities are normalized and vertical offsets were added. The inset to (a) shows an expanded view of the leading edge of the signal at 3.75 mm. The vertical dashed lines show the start and end of the f_p signal at $x = 2.75$ mm. The black arrow in (b) points out the secondary rise feature of the signal.

is strong near the rising edge of the pulse for the first ∼30 ns for all x and then drops abruptly. There is a weaker peak of similar duration (20 ns) at the trailing edge of the pulse that corresponds to a drop in the magnon population below the nonlinear threshold. The initial f_p peak in Fig. 3(a) evolves as a function of x. At small x, the initial peak is a single, sharp peak, but at farther distances, three distinct peaks are observed. The first and strongest peak corresponds to the lowest-order thickness mode, the most efficiently excited mode that also has the highest group velocity, and the additional peaks are most likely slower, higher-order thickness or width-quantized modes. In Fig. 2(a), each solid line represents the dispersion curve for a different thickness mode and each mode has a slightly different group velocity. All of the excited modes undergo splitting, as evidenced by the short duration of the peaks. Aside from the initial peak(s), the temporal profile is otherwise preserved at all distances, indicating that splitting occurs close to the antenna ($x < 2.75$ mm, the closest BLS measurement).

The $f_p/2$ signal [Fig. 3(b)] exhibits a more complex shape evolution as a function of t. Like the f_p signal, an initial ∼30-ns-long peak is observed that is indicative of the time needed to build a sufficient magnon population to support confluence. At $x = 2.75$ mm, this is followed by a slow rise over the course of 400 ns, a relatively flat response, and then a gradual decay (120 ns) followed by an extended tail that persists for >500 ns. At larger x, the initial peak becomes more pronounced and is separated in time from the slow rise by a flat, lower-amplitude section. The origin of this feature will be discussed later. The mid and falling edge features are similar for all x and the slow trailing edge is attributed to the slower magnons that occur near the minimum in the dispersion relation [Fig. 2(a)].

The f_c pulse shape [Fig. 3(c)] remains the same within the noise level for all x aside from an overall delay that increases with x. The signal builds gradually for 290 ± 50 ns, stays flat for the remainder of the microwave pulse, and then diminishes down to the background level over the next 250 ns. There may be a distribution of group velocities but since the pulse shape does not change appreciably with x, the gradual nature of the pulse rise and fall is more likely a reflection of the time it takes to achieve a steady-state population of f_c magnons. The constant pulse shape vs x indicates that the confluence process must also occur close to the antenna ($x < 2.75$ mm). The f_c pulse does show an initial spike, but this is due to bleedthrough from the initially strong f_p signal [see Fig. 2(c)] and the f_c magnons do not appear to undergo further splitting. At later times, the f_c and f_p signals are distinguishable.

To better understand the splitting and confluence processes, the arrival times of key features of the f_p, $f_p/2$, and f_c magnon signals were tracked (Fig. 4). Figure 4(a) shows the arrival times of the initial peak of the f_p magnon signal [Fig. 3(a)] and the initial $f_p/2$ magnons [Fig 3(b)], the time at 10% of the maximum signal along the rising edge. These represent the times at which f_p magnons begin to convert into $f_p/2$ magnons and the arrival time of the first/fastest $f_p/2$ magnons, respectively. Similarly, Fig. 4(b) shows the 10% rise time of the f_c magnons, also along with the initial f_p magnon peak. The uncertainties in the f_p and $f_p/2$ magnon arrival times are taken as the resolution of the time-of-flight analyzer, 2 ns; the uncertainties of the f_c magnon arrival times are larger due to the lower signal to noise [Fig. 3(c)]. Linear fits yield group velocities of $v_{g,x} = 80 \pm 10$ and 16 ± 3 μm/ns for the f_p and $f_p/2$, magnons, respectively, which represent the speeds of the fastest magnons in each case. For the $f_p/2$ magnons, a broad distribution of speeds is expected, which leads to the long signal tail in Fig. 3(b). The intersection of the f_p and $f_p/2$ arrival times in Fig. 4(a) can be used to determine the approximate position where the $f_p/2$ magnons form: $x_0 \leqslant 1.7 \pm 0.2$ mn. The f_c line [Fig. 4(b)] is always delayed with respect to the f_p signal, suggesting that $f_p/2$

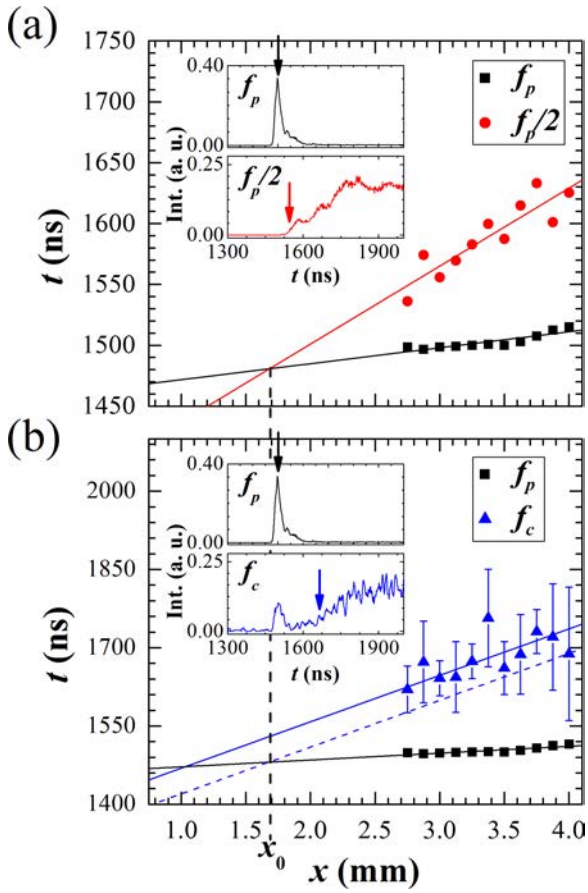

FIG. 4. (a) The arrival times of the maximum f_p signal (black squares), which occur just before the splitting process begins, are shown as a function of x along with the onset (10% rise time) of the $f_p/2$ signal (red circles). Linear fit lines, used to obtain the magnon group velocities, intersect at $x_0 = 1.7 \pm 0.2$ mm. (b) The arrival times of the f_p and f_c magnons, with corresponding linear fits. The two lines intersect at x_0 when a time shift of $t_0 = 90 \pm 170$ ns is applied. The insets show the leading edges of the time-resolved BLS signals at $x = 2.75$ mm.

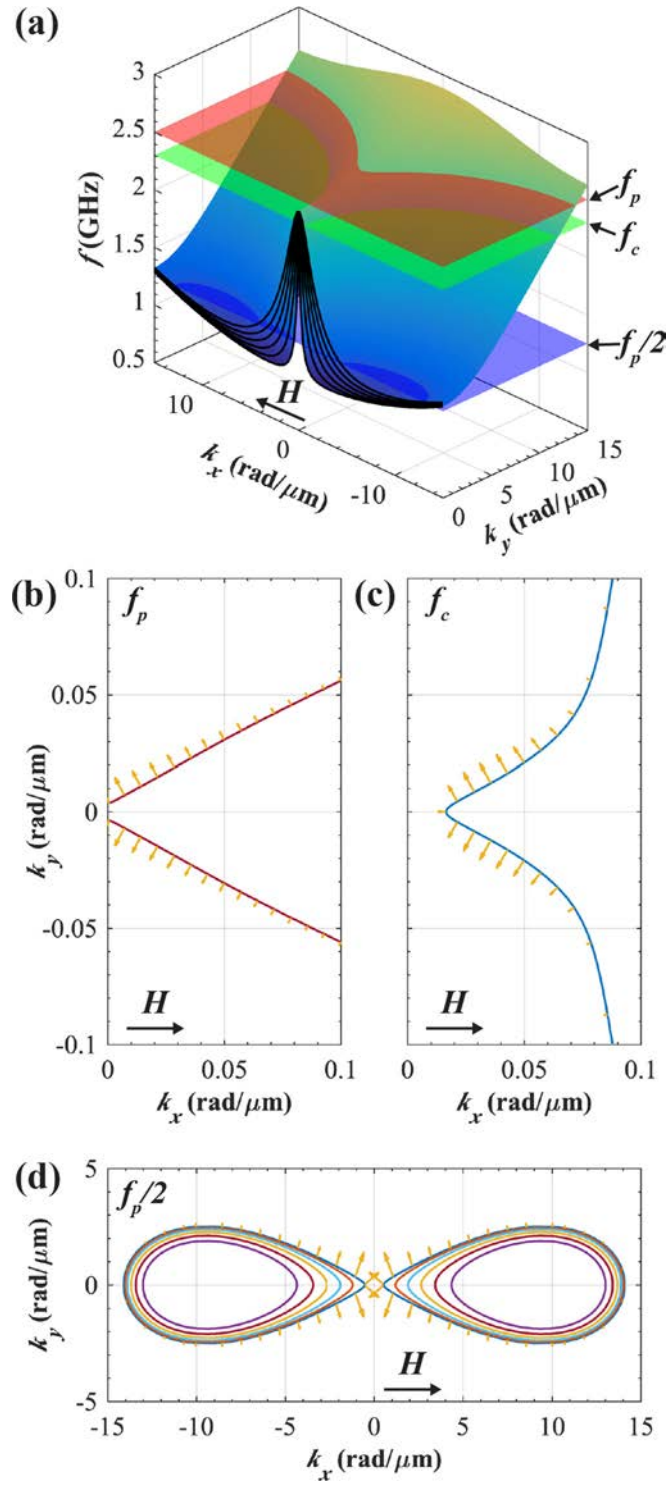

FIG. 5. Calculations of the full dispersion manifold. (a) Surface plots of the magnon frequency vs wave vector along the x and y directions, the backward volume, and surface wave directions in the low-wave-vector magnetostatic regime, respectively, are shown for the first six thickness modes. The red, green, and blue planes in (a) represent f_p, f_c, and $f_p/2$, respectively. The corresponding isofrequency plots are shown in (b)–(d). The solid lines show the permitted wave vectors and the arrows show the group velocities, where the arrow lengths represent the group-velocity magnitudes.

magnons may persist for some period of time, $t_0 \approx 90$ ns, before the f_c magnons begin to form, although there is a large uncertainty in this parameter.

Maximum velocities along the x direction, $v_{g,x}$, were obtained from the gradients of the full spin-wave dispersion surfaces (Fig. 5). These calculations were also done using the dipole-exchange theory [20] and the same parameters as for Fig. 2(a). Isofrequency cuts show the distribution of allowed wave vectors at f_p, $f_p/2$, and f_c as well as the associated group velocities. The predicted maximum $v_{g,x}$ are 107, 4.4, and 52 μm/ns for the f_p, $f_p/2$, and f_c magnons, respectively. The agreement with the measured values is not perfect, but $v_{g,x}$ is appreciably smaller for the $f_p/2$ magnons as compared to the f_p magnons, which qualitatively agrees with the experiment. For the $f_p/2$ magnons, although the zero-velocity magnons will not propagate, many of the slower magnons will, which explains the extended tail observed in the $f_p/2$ signal [Fig. 3(b)]. The BLS is not sensitive to the

high-wave-vector exchange magnons so the fastest observed velocities are due to the low-wave-vector magnons.

One of the features in the time-resolved BLS signals that is not explained by the dispersion relations alone is the flat section on the rising edge of the $f_p/2$ signal that directly follows the initial peak [Fig. 3(b)]. A simple model was employed to understand the effects of the range of excited velocities and the confluence process on the pulse shape. Magnon pulses with velocities of $0-16\,\mu$m/ns were propagated as a function of x and summed assuming that a fraction n_c of the $f_p/2$ magnons is lost to the confluence process after the first 30 ns, the approximate duration of the first peaks of both the f_p and $f_p/2$ signals. Confluence was assumed to occur close to the antenna because this is where the population of $f_p/2$ magnons is high enough to lead to significant confluence. As previously mentioned, the fact that the shape of the f_c signal [Fig. 3(c)] does not change as a function of x supports this assumption. Damping appropriate for YIG was also included. Various models for the conversion efficiency as a function of $v_{g,x}$ were considered that involved (i) uniform confluence efficiencies with n_c ranging from 0 to 0.95, and (ii) a two-step model, with $n_c(v_{g,x}) = n_{c1}$ for $v_{g,x} < v_t$ and $n_c(v_{g,x}) = n_{c2}$ for $v_{g,x} > v_t$, where transition speeds v_t of between 0 and 16 μm/ns were considered and each of n_{c1} and n_{c2} was varied from 0 to 0.95. Two representative results are shown in Fig. 6. A uniform confluence efficiency, for any $n_c > 0$, produces a pulse with an initial peak followed by a flat region [Fig. 6(a)], but there is no secondary rise. A nonuniform confluence efficiency where the faster magnons have a higher probability of undergoing confluence [$n_{c2} > n_{c1}$, Fig. 6(b)] is required to reproduce the initial peak, flat region, and secondary rise that is observed experimentally [Fig. 3(b)]. The exact shape of the output signal varies depending on the choices of n_{c2}, n_{c1}, and v_t, but the flat region and secondary rise are always present when $n_{c2} > n_{c1}$ and are not present for $n_{c2} \leqslant n_{c1}$. The effect of the initial velocity distribution was also considered, where flat, Gaussian, and bimodal velocity distributions were used. Changes to the initial velocity distribution lead to modifications of the rising and falling edge shapes, and high confluence probabilities produce a two-step decay feature on the falling edge, similar to what is seen in Fig. 3(b). In all cases, however, a velocity-dependent efficiency with $n_{c2} > n_{c1}$ is needed to produce the secondary rise. This model is overly simplistic; nevertheless, it provides insight into the origin of this feature of the $f_p/2$ signal.

Based on the fact that $f_c < f_p$, it would be natural to assume that the lowest-energy magnons are more likely to recombine with each other, but these are also the magnons with the lowest group velocities and the data indicate that the probability of confluence is, in fact, higher for the magnons with the higher v_{gx}. This may indicate that the lowest-velocity $f_p/2$ magnons have a higher probability of relaxing into a condensate than undergoing confluence, and that the magnons that do combine also undergo additional processes that involve energy loss while they are part of the split magnon population. Since the splitting and confluence cross sections should depend on temperature [15], temperature-dependent measurements could yield additional insight into these processes.

In summary, time-resolved BLS measurements of the nonlinear magnon splitting and confluence processes show that both of these processes occur close to the microwave antenna. The data show that the f_p magnons undergo splitting with a high efficiency after a delay of ~30 ns and within a distance of 1.7 ± 0.2 mm of the antenna, the $f_p/2$ magnons commence confluence on a similar timescale, and the f_c magnons do not undergo further splitting once created. Furthermore, the shape of the $f_p/2$ signal suggests that the confluence efficiency is higher for the magnons that have faster group velocities, which raises new questions. Further theoretical work in this area is needed to develop a complete picture of the splitting and confluence processes, and to answer the question of why the confluence efficiency varies with group velocity.

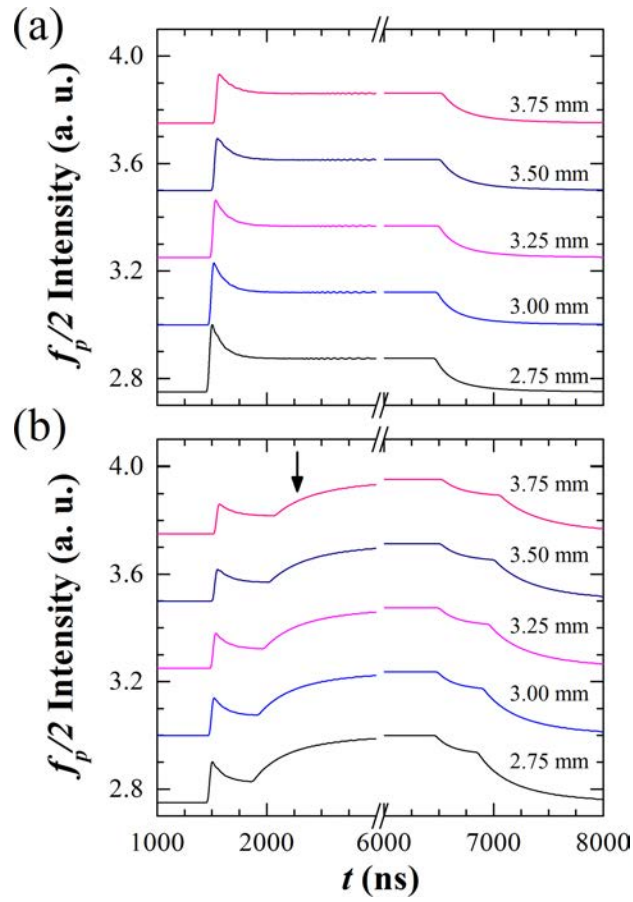

FIG. 6. Models of the expected $f_p/2$ signal shape calculated for (a) a velocity-independent conversion efficiency from $f_p/2$ to f_c (95%) and (b) a velocity-dependent conversion efficiency with a 95% efficiency for $v_{g,x}$ of 5 to 16 μm/ns and 25% for lower $v_{g,x}$. The black arrow in (b) points out the secondary rise feature of the pulse that is absent in (a).

The authors would like to thank Dr. Helmut Schultheiss and Dr. Katrin Schultheiss for their advice on time-resolved BLS. This research was supported by the US Department of Energy, Office of Basic Energy Sciences, Division of Materials Sciences and Engineering under Award No. ER 46854 (experiments, CSU), NSF Grant No. EFMA-1741666 (calculations, CSU), UNAM-DGAPA Grant No. 1N107318, UNAM PIIF "Magnón-espintrónica en medios metálicos y dieléctricos" (work at UNAM), and the Russian Science Foundation Grant No. 14-12-01296-P (work at LETI).

[1] N. Bloembergen and S. Wang, Phys. Rev. **87**, 392 (1952).
[2] P. E. Wigen, *Nonlinear Phenomena and Chaos in Magnetic Materials* (World Scientific, Singapore, 1994).
[3] S. O. Demokritov, V. E. Demidov, O. Dzyapko, G. A. Melkov, A. A. Serga, B. Hillebrands, and A. N. Slavin, Nature (London) **443**, 430 (2006).
[4] P. W. Anderson and H. Suhl, Phys. Rev. **100**, 1788 (1955).
[5] H. Suhl, Proc. IRE **44**, 1270 (1956).
[6] H. Suhl, J. Phys. Chem. Solids **1**, 209 (1957).
[7] K. Ando, T. An, and E. Saitoh, Appl. Phys. Lett. **99**, 092510 (2011).
[8] H. Kurebayashi, O. Dzyapko, V. E. Demidov, D. Fang, A. J. Ferguson, and S. O. Demokritov, Appl. Phys. Lett. **99**, 162502 (2011).
[9] C. W. Sandweg, Y. Kajiwara, A. V. Chumak, A. A. Serga, V. I. Vasyuchka, M. B. Jungfleisch, E. Saitoh, and B. Hillebrands, Phys. Rev. Lett. **106**, 216601 (2011).
[10] K. Ando and E. Saitoh, Phys. Rev. Lett. **109**, 026602 (2012).
[11] H. Sakimura, T. Tashiro, and K. Ando, Nat. Commun. **5**, 5730 (2014).
[12] S. A. Manuilov, C. H. Du, R. Adur, H. L. Wang, V. P. Bhallamudi, F. Y. Yang, and P. C. Hammel, Appl. Phys. Lett. **107**, 042405 (2015).
[13] T. Tashiro, S. Matsuura, A. Nomura, S. Watanabe, K. Kang, H. Sirringhaus, and K. Ando, Sci. Rep. **5**, 15158 (2015).
[14] V. Lauer *et al.*, Appl. Phys. Lett. **108**, 012402 (2016).
[15] A. N. Anisimov and A. G. Gurevich, Sov. Phys. Solid State **18**, 20 (1976) [Fiz. Tverd. Tela **18**, 38 (1976)].
[16] A. G. Gurevich and G. A. Melkov, *Magnetization Oscillations and Waves* (CRC, Boca Raton, FL, 1996).
[17] C. Mathieu, V. T. Synogatch, and C. E. Patton, Phys. Rev. B **67**, 104402 (2003).
[18] C. L. Ordonez-Romero, B. A. Kalinikos, P. Krivosik, W. Tong, P. Kabos, and C. E. Patton, Phys. Rev. B **79**, 144428 (2009).
[19] O. Büttner, M. Bauer, S. O. Demokritov, B. Hillebrands, Y. S. Kivshar, V. Grimalsky, Y. Rapoport, and A. N. Slavin, Phys. Rev. B **61**, 11576 (2000).
[20] B. A. Kalinikos and A. N. Slavin, J. Phys. C Solid State **19**, 7013 (1986).
[21] D. D. Stancil and A. Prabhakar, *Spin Waves: Theory and Applications* (Springer, New York, 2009).
[22] W. Wettling, M. G. Cottam, and J. R. Sandercock, J. Phys. C Solid State **8**, 211 (1975).
[23] V. T. Synogach, Y. K. Fetisov, C. Mathieu, and C. E. Patton, Phys. Rev. Lett. **85**, 2184 (2000).